

A Fabric Material Model with Stress Map Functionality in LS-DYNA

Thomas Borrvall¹, Curtis Ehle², Troy Stratton²

¹DYNAmore Nordic AB, Linköping, Sweden

²Autoliv OTC, Ogden UT, USA

1 Introduction

Woven fabric behavior is generally highly non-linear and non-isotropic. Such behavior is difficult to approximate with typical continuum based material models. As such, woven fiber behavior has generally been simulated employing simple uncoupled non-linear orthotropic behavior based on uniaxial or equi-biaxial input. This approach has been acceptable for system level modeling of airbag-occupant interaction as well as modeling of general inflated shape and volume but insufficient for reasonably accurate prediction of local stress states within the cushion. The stress state can be used as an indicator of failure in seams and thus used to assess the constructional design of the airbag.

Historically, LS-DYNA [1] has provided a number of options for modeling of fabric, all connected to the keyword MAT_FABRIC. This material model assumes that the fabric can be modeled as a membrane without bending resistance and provides a collection of features associated with airbag modeling. From a pure constitutive viewpoint, FORM=14 provides non-linear uncoupled fiber behavior. Stress-strain response is based on either uniaxial, equi-biaxial input or some selected strain state in between. This approach can provide approximation of general material stiffness due to fiber coupling but only for the immediate domain of the selected input. FORM=-14 was subsequently developed and partially incorporates stiffness effects of fiber coupling over a limited but larger domain. This is accomplished by input of both uni-axial and equi-biaxial input and linearly interpolating between, thereby reasonably approximating fiber coupling for a limited domain near equi-biaxial behavior.

The subject of this paper is a new fabric model, MAT_FABRIC_MAP which is a general approach to model fiber coupling effects for the entire tension-tension domain while allowing for uncoupled behavior in the compression-tension and compression-compression domains. This is accomplished via direct mapping (tables) of fiber stresses to corresponding warp and weft fiber strain points throughout the strain domain of simulation. The approach is discussed in comparison with alternate approaches and along with numerical and physical considerations that were addressed to ensure solution stability.

The paper is organized as follows. In Section 2 and 3 the theory of three variants of the LS-DYNA fabric material model is presented together with accompanying parameter estimation approaches. The physics behind the different approaches is discussed. Some additional features required for robustness and accuracy in airbag simulations are presented in Sections 4 and 5, in particular an optional bending resistance that can be used for a controlled behavior of the fabric. Some examples from the airbag industry are provided in Section 6 and the paper concludes with a summary in Section 7.

2 The Fabric Material Models

Throughout this paper we repeatedly use E , E_x , E_{xx} , E_{yy} and E_{xy} to denote Green strain data and likewise S , S_x , S_{xx} , S_{yy} and S_{xy} to denote 2nd Piola-Kirchhoff stress data.

2.1 FORM=14

FORM=14 is probably the most common option in everyday simulation of material 34 (MAT_FABRIC). It allows for specification of input curves to define individual stress components' response as function of corresponding strain components

$$S_{xx} = S_{xx}(E_{xx}) \quad (1a)$$

$$S_{yy} = S_{yy}(E_{yy}) \quad (1b)$$

$$S_{xy} = S_{xy}(E_{xy}). \quad (1c)$$

The first two curves can in principle be estimated directly from two uniaxial tests, see top of Figure 1, as follows. For a sample specimen of length l and cross sectional area A , let $f(d)$ be the force displacement curve from the test. Then the uniaxial strain and stress used in the material model is calculated as

$$E = \frac{1}{2} \left(\frac{d}{l} + 1 \right)^2 - \frac{1}{2} \quad (2a)$$

$$S = \frac{f(d)}{A} \frac{l}{l+d} \quad (2b)$$

but this approach typically results in too soft response in airbag applications. Therefore an approach is used that incorporates biaxial effects, see bottom of Figure 1. The shear curve estimation is treated in detail in Section 3.



Figure 1 Uniaxial (top) and biaxial (bottom) test setup.

2.2 FORM=-14

To account for biaxial stiffening, FORM=-14 was developed. The stress is here determined from a set of uniaxial and biaxial input curves

$$S_{XX} = \left(1 - \alpha\left(\frac{E_{YY}}{E_{XX}}\right)\right) S_{XX}^u(E_{XX}) + \alpha\left(\frac{E_{YY}}{E_{XX}}\right) S_{XX}^b(E_{XX}) \quad (3a)$$

$$S_{YY} = \left(1 - \alpha\left(\frac{E_{XX}}{E_{YY}}\right)\right) S_{YY}^u(E_{YY}) + \alpha\left(\frac{E_{XX}}{E_{YY}}\right) S_{YY}^b(E_{YY}) \quad (3b)$$

while the shear stress is the same as in FORM=14, see (1c). These formula are valid only for $E_{XX} > 0$ and $E_{YY} > 0$, for other combinations of strain (1a) and (1b) are used. The function α used to interpolate between the uniaxial and biaxial curves can be expressed simply as

$$\alpha(q) = \min(1, q). \quad (4)$$

The curves can be estimated from uniaxial and biaxial tests, see Figure 1, and the resulting model is accounting for biaxial stiffening due to interaction between yarns in the warp and weft directions. Unfortunately the heterogeneous strain distribution in the biaxial test prevents using formulas like (2) for the biaxial curves, and a more sophisticated approach is required.

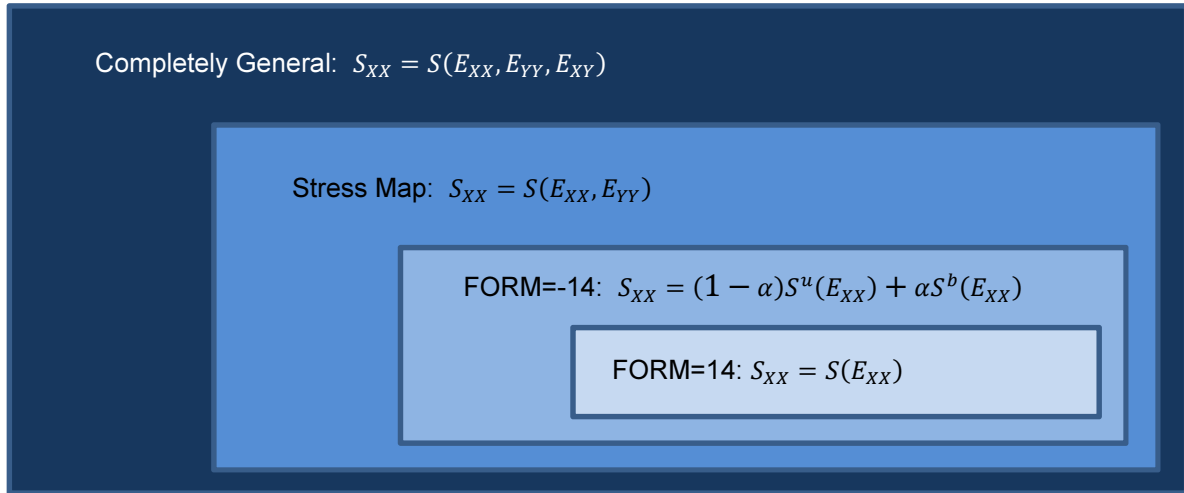


Figure 2 Illustration of the generality of different fabric models, FORM=14 is incorporated in FORM=-14, which in turn is incorporated in the Stress Map material.

2.3 Stress Map

The Stress Map Material, as the name suggests, maps a point in strain space to a point in stress space. A utopian goal would in general be to prescribe a function

$$\mathbf{S} = \mathbf{S}(\mathbf{E}). \quad (5)$$

For practical purposes this is somewhat specialized and broken down into expressions involving individual components of stress and strain. For the user's convenience they are expressed in engineering quantities, we have

$$P_{XX} = P_{XX}(e_{XX}, e_{YY}) \quad (6a)$$

$$P_{YY} = P_{YY}(e_{YY}, e_{XX}) \quad (6b)$$

where e_{XX} and e_{YY} denote the engineering strain components while P_{XX} and P_{YY} are the engineering stress components. The conversion formulae between the stress and strain measures used are

$$e = \sqrt{1 + 2E} - 1 \quad (7a)$$

$$S = \frac{P}{1 + e} \quad (7b)$$

and are applied in the two fiber directions. This model is a generalization of FORM=-14 and the most general elastic model for fabrics currently available.

One nice feature with the stress map approach, that is not incorporated in the elastic models of FORM=14 or FORM=-14, is nonlinear Poisson effects. Using the former models, deformation in uniaxial strain in either warp or weft direction will inevitably result in a uniaxial stress response. Referring to Figure 3, the tables used in the Stress Map model can be set up so that uniaxial strain will result in a contractive stress, resulting in a realistic response of a fabric in uniaxial tension.

Weft 2nd P-K Stress as a function of Green's Strains

		Warp Strain (Green's)																				
		-0.37500	-0.34875	-0.32000	-0.28875	-0.25500	-0.21875	-0.18000	-0.13875	-0.09500	-0.04875	0.00000	0.05126	0.10500	0.16125	0.22001	0.28125	0.34501	0.41125	0.48000	0.55125	0.62500
Weft Strain (Green's)	-0.37500	-150.000	-150.000	-150.000	-150.000	-150.000	-150.000	-150.000	-150.000	-150.000	-150.000	-150.000	-135.0	-123.0	-111.0	-99.0	-93.0	-90.0	-90.0	-90.0	-90.0	-90.0
	-0.34875	-122.727	-122.727	-122.727	-122.727	-122.727	-122.727	-122.727	-122.727	-122.727	-122.727	-122.7	-109.1	-98.2	-87.3	-76.4	-70.9	-68.2	-68.2	-68.2	-68.2	-68.2
-0.32000	-100.000	-100.000	-100.000	-100.000	-100.000	-100.000	-100.000	-100.000	-100.000	-100.000	-100.000	-100.0	-87.5	-77.5	-67.5	-57.5	-52.5	-50.0	-50.0	-50.0	-50.0	-50.0
-0.28875	-80.769	-80.769	-80.769	-80.769	-80.769	-80.769	-80.769	-80.769	-80.769	-80.769	-80.8	-80.8	-69.2	-60.0	-50.8	-41.5	-36.9	-34.6	-34.6	-34.6	-34.6	-34.6
-0.25500	-64.286	-64.286	-64.286	-64.286	-64.286	-64.286	-64.286	-64.286	-64.286	-64.286	-64.3	-64.3	-53.6	-45.0	-36.4	-27.9	-23.6	-21.4	-21.4	-21.4	-21.4	-21.4
-0.21875	-50.000	-50.000	-50.000	-50.000	-50.000	-50.000	-50.000	-50.000	-50.000	-50.000	-50.0	-50.0	-40.0	-32.0	-24.0	-16.0	-12.0	-10.0	-10.0	-10.0	-10.0	-10.0
-0.18000	-37.500	-37.500	-37.500	-37.500	-37.500	-37.500	-37.500	-37.500	-37.500	-37.500	-37.5	-37.5	-28.1	-20.6	-13.1	-5.6	-1.9	0.0	0.0	0.0	0.0	0.0
-0.13875	-26.471	-26.471	-26.471	-26.471	-26.471	-26.471	-26.471	-26.471	-26.471	-26.471	-26.5	-26.5	-17.6	-10.6	-3.3	4.1	9.5	10.8	11.5	12.4	13.2	14.1
-0.09500	-16.667	-16.667	-16.667	-16.667	-16.667	-16.667	-16.667	-16.667	-16.667	-16.667	-16.7	-16.7	-8.3	-1.7	10.3	19.9	24.6	26.5	28.3	30.4	32.5	34.7
-0.04875	-7.895	-7.895	-7.895	-7.895	-7.895	-7.895	-7.895	-7.895	-7.895	-7.895	-7.9	-7.9	0.0	16.9	29.9	43.6	48.7	48.4	48.4	49.2	49.9	50.5
0.00000	0.000	0.000	0.000	0.000	0.000	0.000	0.000	0.000	0.000	0.000	0.0	0.0	18.3	30.1	53.1	59.0	64.7	60.2	70.2	70.7	72.0	72.0
0.05126	19.524	19.524	19.524	19.524	19.524	19.524	19.524	19.524	19.524	19.524	20.0	21.5	40.0	69.0	80.0	97.3	106.6	109.4	110.4	111.3	112.6	114.3
0.10500	41.818	41.818	41.818	41.818	41.818	41.818	41.818	41.818	41.818	41.818	43.9	52.5	72.7	91.1	107.4	123.8	134.4	139.2	140.9	141.6	143.2	145.4
0.16125	84.348	84.348	84.348	84.348	84.348	84.348	84.348	84.348	84.348	84.348	85.191	88.6	91.9	108.5	122.5	137.1	152.5	159.0	159.0	160.8	162.5	164.7
0.22001	131.666	131.666	131.666	131.666	131.666	131.666	131.666	131.666	131.666	131.666	132.982	138.2	148.1	161.3	178.8	182.6	191.6	195.0	193.3	196.7	199.6	200.0
0.28125	152.000	152.000	152.000	152.000	152.000	152.000	152.000	152.000	152.000	152.000	154.061	160.1	172.2	186.5	199.4	209.3	217.8	227.9	234.8	237.2	237.6	239.0
0.34501	155.943	155.943	155.943	155.943	155.943	155.943	155.943	155.943	155.943	155.943	157.502	163.7	175.4	191.0	205.8	220.7	233.9	250.9	265.5	269.5	269.6	272.2
0.41125	157.071	157.071	157.071	157.071	157.071	157.071	157.071	157.071	157.071	157.071	158.535	164.8	176.4	192.4	210.6	228.4	247.5	265.3	279.1	286.1	290.0	293.9
0.48000	158.117	158.117	158.117	158.117	158.117	158.117	158.117	158.117	158.117	158.117	159.698	166.0	177.9	193.7	213.9	232.7	251.0	271.1	282.2	292.3	300.4	305.4
0.55125	159.091	159.091	159.091	159.091	159.091	159.091	159.091	159.091	159.091	159.091	160.715	167.1	179.1	194.9	213.6	232.0	253.3	268.6	281.2	293.7	303.9	310.4
0.62500	160.000	160.000	160.000	160.000	160.000	160.000	160.000	160.000	160.000	160.000	161.700	168.0	180.0	196.0	211.7	228.7	246.0	270.0	278.8	293.7	304.0	311.7

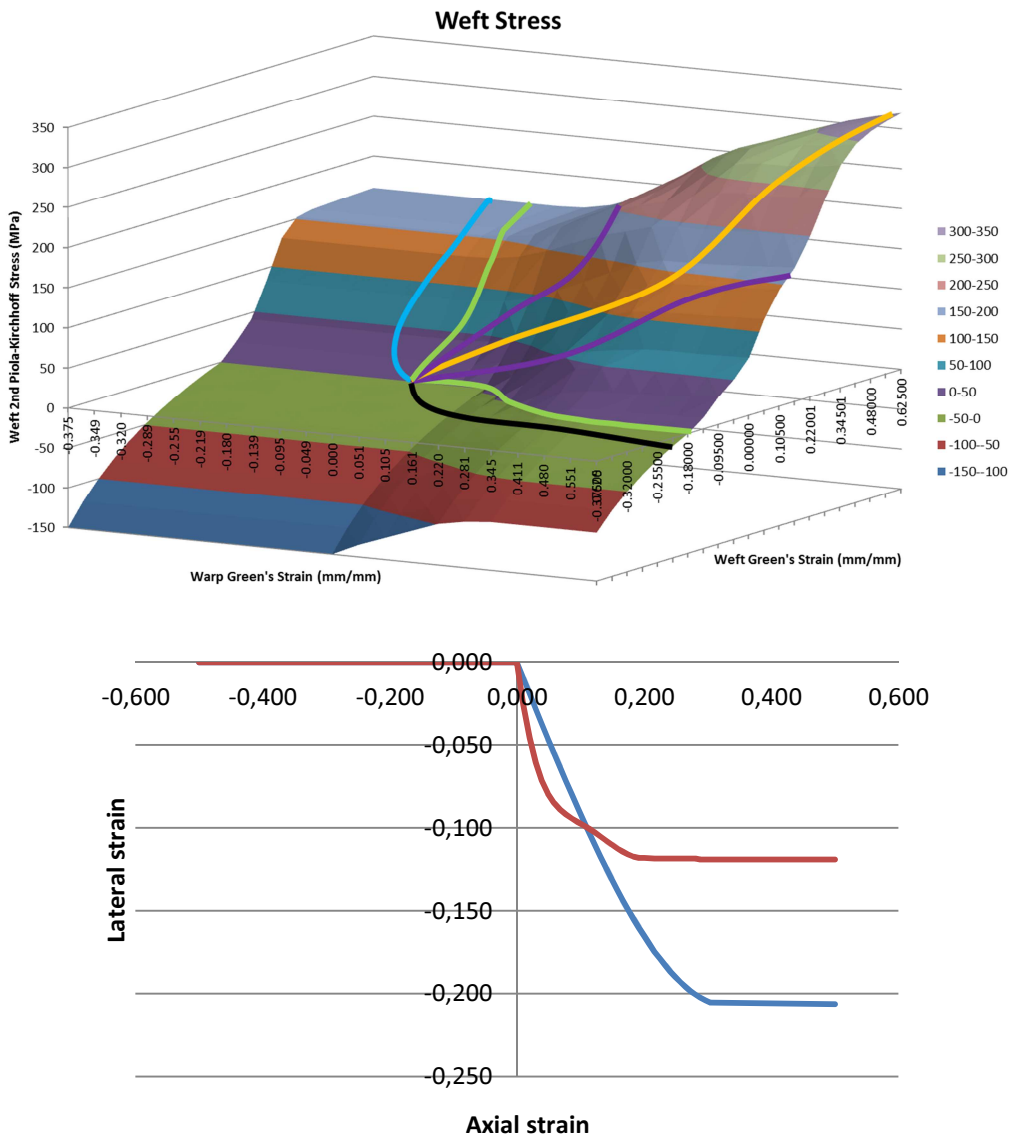


Figure 3 Excel input of weft stress table and resulting weft stress surface, some special stress strain paths are indicated. The effect of nonlinear Poisson's ratio is illustrated below for uniaxial deformation in warp and weft directions.

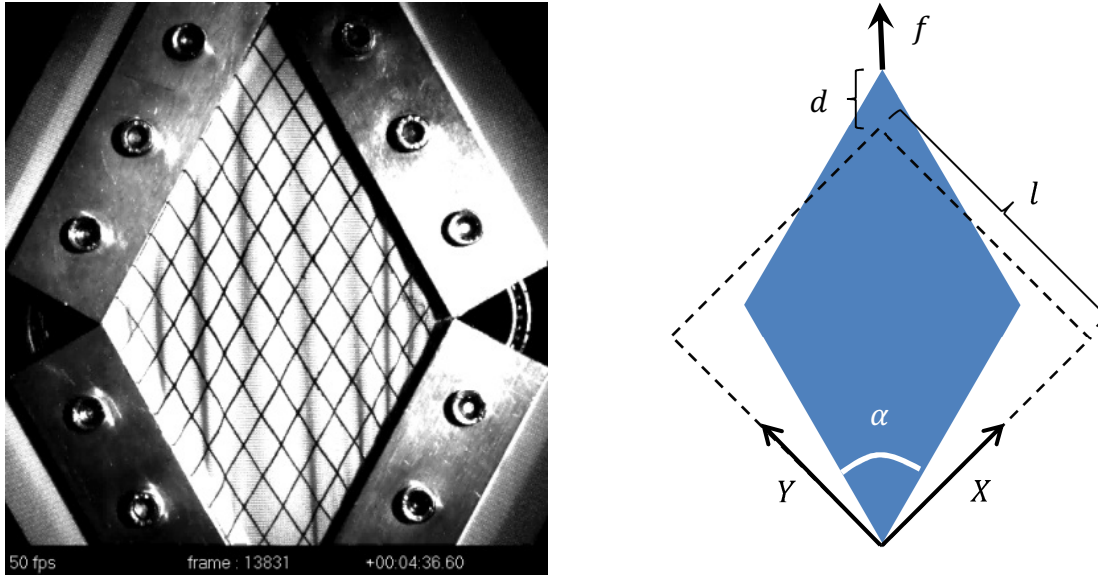


Figure 4 Wrinkling in the picture frame test due to compaction of fibers. Data for shear curve estimation is shown to the right.

3 The Picture Frame Test for Shear

To estimate the shear curve in either one of the three material models in the previous Section, the picture frame test is used. This is illustrated in Figure 4, a piece of fabric is inserted into a frame and sheared by displacing two opposite hinge points which results in a perfect shear of the specimen. The shear test is performed by attaching a quadratic piece of fabric to a rigid frame and pulling one of the corners of the frame so that the fabric deforms according to Figure 4. The corner point is displaced an amount d in the direction of the applied force, where the force with magnitude $f(d)$ is directed along the diagonal of the deformed fabric. To determine the stress-strain curve, we use the principle of energy conservation, see right of Figure 4 for the following.

The variation of external work by the force can be expressed as

$$\delta W_e = f(d)\delta d, \quad (8)$$

and should equilibrate the corresponding variation of the internal work in the fabric. This is derived as follows. The deformation of the fabric is described by

$$x = X + Y \cos \alpha \quad (9a)$$

$$y = Y \sin \alpha \quad (9b)$$

and the deformation gradient is given by

$$\mathbf{F} = \begin{bmatrix} 1 & \cos \alpha \\ 0 & \sin \alpha \end{bmatrix} \quad (10)$$

The Green-Lagrange strain is expressed in terms of the angle α as

$$\mathbf{E} = \frac{1}{2} \begin{bmatrix} 0 & \cos \alpha \\ \cos \alpha & 0 \end{bmatrix} \quad (11)$$

and the second Piola-Kirchoff shear stress is a function of the Green-Lagrange shear strain, i.e.,

$$S_{XY} = S_{XY} \left(\frac{\cos \alpha}{2} \right) \quad (12)$$

The variation of the internal work can be expressed as

$$\delta W_i = 2 \int_{\Omega_0} S_{XY} \frac{\partial E_{XY}}{\partial d} d\Omega_0 \delta d = -l^2 t \sin \alpha \frac{\partial \alpha}{\partial d} S_{XY} \left(\frac{\cos \alpha}{2} \right) \delta d \quad (13)$$

where t is the thickness of the fabric and l is the length of the sides. The displacement d can be expressed in terms of the shear angle α as

$$d = l \left(2 \cos \frac{\alpha}{2} - \sqrt{2} \right) \quad (14)$$

and differentiating this expression implicitly gives

$$\frac{\partial \alpha}{\partial d} = - \frac{1}{l \sin \frac{\alpha}{2}} \quad (15)$$

The final expression of the internal work variation becomes

$$\delta W_i = 2 l t \cos \frac{\alpha}{2} S_{XY} \left(\frac{\cos \alpha}{2} \right) \delta d. \quad (16)$$

Since the variation of the internal work is equal to the variation of the external work, we get

$$f(d) = 2 l t \cos \frac{\alpha}{2} S_{XY} \left(\frac{\cos \alpha}{2} \right) \quad (17)$$

or when substituting α we get the following shear data pairs

$$E_{XY} = \frac{1}{2} \left(\left\{ \frac{d}{l\sqrt{2}} + 1 \right\}^2 - 1 \right) \quad (18a)$$

$$S_{XY} = \frac{f(d)}{t(l\sqrt{2} + d)} \quad (18b)$$

The reason for using energy conservation in the derivation of the stress-strain curve is due to the presence of the rigid frame that resists the fabric from deforming. Using a force equilibrium principle is problematic since the rigid frame sustains much of the load. The magnitude of this load is unknown and must be treated correctly in a force equilibrium equation. However, the rigid frame does not store energy, hence the energy principle is the preferred choice.

Assuming that the fabric remains planar with respect to the picture frame, it is reasonable to assume

$$f(d) \rightarrow \infty \text{ when } d \rightarrow \sqrt{2}(\sqrt{2} - 1)l \quad (19)$$

and the elastic model thus predicts

$$S_{XY} \rightarrow \infty \text{ when } E_{XY} \rightarrow 1/2 \quad (20)$$

but the shear data curves normally used in fabric material data typically never implements this. A consequence of the conventional approach is that the effect of packing of yarns as the volume decreases is not captured properly. It can be debated how this is adequately modelled, but we choose to see this as a volumetric effect not necessarily pertinent to shear deformation but to any volume reductive deformation. So the shear curve is essentially used to estimate the shear response for small to moderate strains, but when the jacobian $J = \det(\mathbf{F})$ becomes smaller than some critical value J_c , the pressure is increased by an additional term. In mathematical terms this packing term can be written

$$p = K_c \ln \left(\frac{J_c}{J} \right), \text{ for } J \leq J_c \quad (21)$$

where K_c is a bulk modulus used for the purpose. The violation of (20) is closely connected to the general draw-backs of a Kirchhoff St Venant hyperelastic material in compression, which is also remedied by augmentations resulting in infinite elastic energy for vanishing volume, see [2].

A piece of fabric can be seen as a composition of air (void) and dense woven material (solid) that by a homogenization argument is modelled as a continuum. From this viewpoint, the physical interpretation of J_c would be the volume ratio of the solid to the homogenized material. When deformed volumetrically there is little resistance until all air is gone and the fabric is solidified, then the compaction kicks in. As mentioned above this is not just pertinent to shear deformation, for uniaxial compression the same physical phenomenon takes place and (21) essentially replaces steep slopes

in the uniaxial compression curves. In Figure 5 the simulated wrinkling in the picture frame test is shown in comparison to a complete fold up of a model without compaction stiffening.

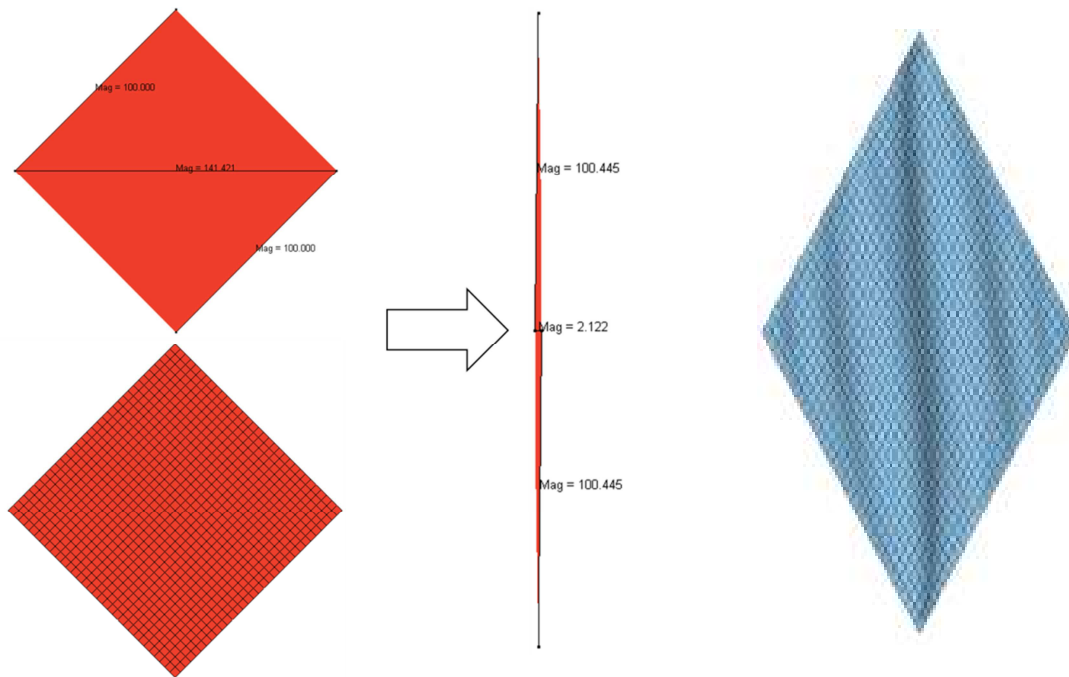


Figure 5 Simulation result of picture frame test without and with compaction.

4 Resolution of Dynamic Instabilities

4.1 Must Elastic Materials be Hyperelastic?

A hyperelastic material is characterized by either one of the three equivalent statements

1. The stress \mathbf{S} is derived from an elastic energy potential $W(\mathbf{E})$, $\mathbf{S} = \frac{\partial W}{\partial \mathbf{E}}$.
2. The work done by the material in an arbitrary closed cycle is zero, $\oint \mathbf{S} : d\mathbf{E} = 0$.
3. The material tangent modulus has major symmetry, $\mathbf{A} : \frac{\partial \mathbf{S}}{\partial \mathbf{E}} : \mathbf{B} = \mathbf{B} : \frac{\partial \mathbf{S}}{\partial \mathbf{E}} : \mathbf{A}$ for arbitrary \mathbf{A} and \mathbf{B} .

From this, it can be concluded from analysis of fabric materials that FORM=14 is hyperelastic while FORM=-14 and Stress Map in general are not. While this seems more of an academic detail, it will be shown that there are significant practical consequences in the simulation of the three materials. In Figure 6, the simulation under study is shown, an inflation of a mushroom airbag. Starting from a flat configuration, the airbag is pressurized during the first 50 ms and after that the pressure is kept constant for the remainder of the simulation. Despite using reasonable elastic material data for all three materials, albeit including coupling effects for the latter two, only FORM=14 yields a stable simulation. This is illustrated in Figure 7, showing that the energy balance deteriorates for FORM=-14 and Stress Map. In what follows, we show that thermodynamics provides a reason to assume that an elastic material must be hyperelastic, and we believe this is the reason for the observed dynamic instabilities. As a reference, the problem has been treated in e.g. [3].

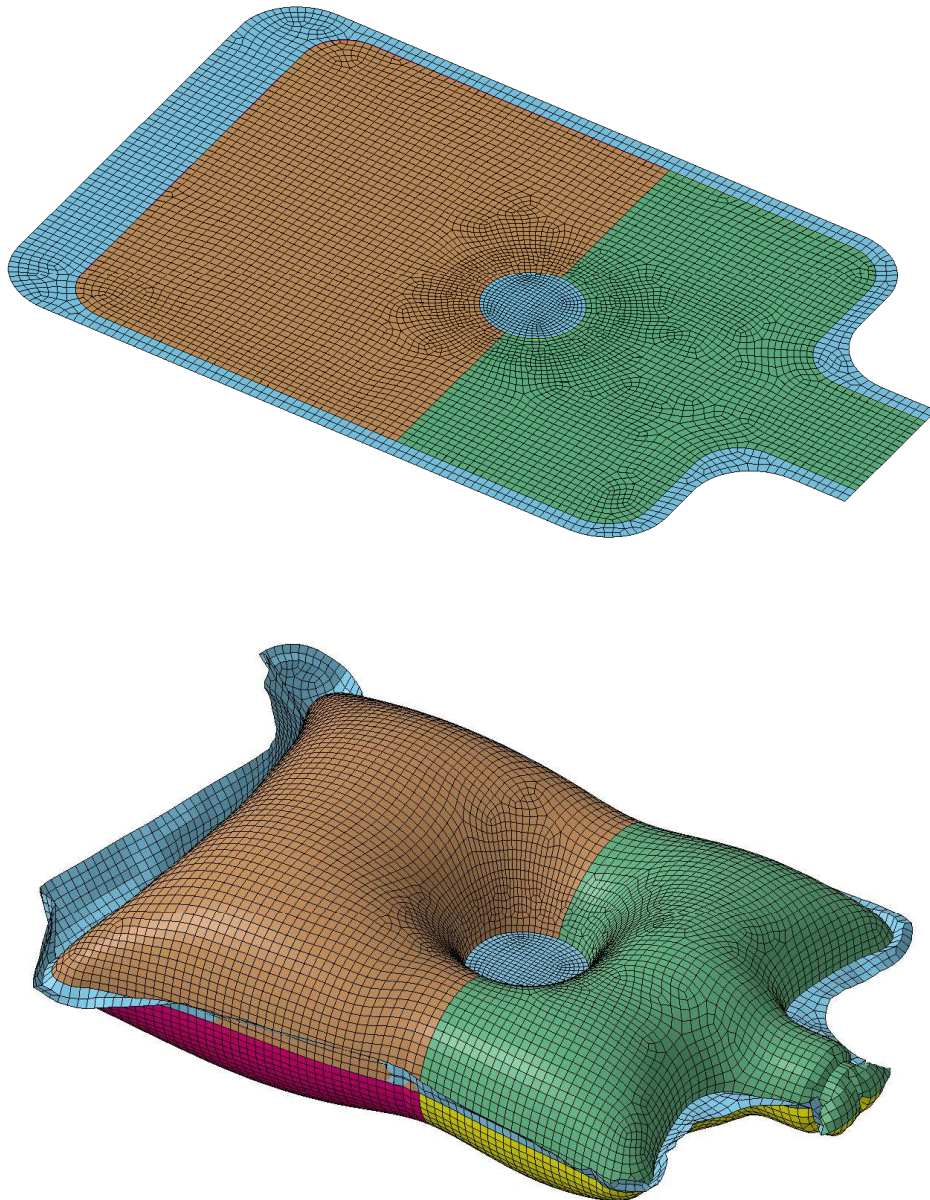


Figure 6 Inflation of mushroom airbag.

Consider a body \mathcal{B} occupying the domain Ω_0 at time zero. The equations of motion can be written

$$\dot{K} + \int_{\Omega_0} \mathbf{S} : \dot{\mathbf{E}} d\Omega_0 = P \quad (22)$$

where K is the kinetic energy and P is the external power. The first law of thermodynamics states that energy cannot be created or destroyed, and is mathematically written as

$$\int_{\Omega_0} \rho_0 \dot{e} d\Omega_0 = \int_{\Omega_0} \mathbf{S} : \dot{\mathbf{E}} d\Omega_0 + \int_{\Omega_0} \rho_0 r d\Omega_0 - \int_{\partial\Omega_0} \mathbf{q}_0 \cdot \mathbf{n}_0 d\partial\Omega_0, \quad (23)$$

where ρ_0 is the material density, $e = e(\mathbf{E}, \theta)$ is the specific internal energy, r is the heat supply per unit mass and $\mathbf{q}_0 \cdot \mathbf{n}_0$ is the heat flux across the boundary of \mathcal{B} . Furthermore, the second law of thermodynamics essentially says that the dissipation must be positive, i.e., the work performed by a system can at most be equal to the energy put in. This can be expressed as Clausius' inequality for an arbitrary cyclic process

$$\oint \left\{ \int_{\Omega_0} \frac{\rho_0 r}{\theta} d\Omega_0 - \int_{\partial\Omega_0} \frac{\mathbf{q}_0 \cdot \mathbf{n}_0}{\theta} d\partial\Omega_0 \right\} \leq 0, \quad (24)$$

where θ is the temperature. We restrict ourselves to isothermal processes, i.e., the temperature θ is constant. Integration of the first law (23) for a cyclic process results in

$$\oint \int_{\Omega_0} \mathbf{S} : \dot{\mathbf{E}} d\Omega_0 = - \oint \left\{ \int_{\Omega_0} \rho_0 r d\Omega_0 - \int_{\partial\Omega_0} \mathbf{q}_0 \cdot \mathbf{n}_0 d\partial\Omega_0 \right\}, \quad (25)$$

and by using Clausius' inequality (24) for the right hand side in (25) we get

$$\oint \int_{\Omega_0} \mathbf{S} : \dot{\mathbf{E}} d\Omega_0 \geq 0. \quad (26)$$

If we use (26) in (22) for $P = 0$, i.e., no external forces, we can deduce that the kinetic energy for a cyclic deformation must decrease

$$\Delta K = - \oint \int_{\Omega_0} \mathbf{S} : \dot{\mathbf{E}} d\Omega_0 \leq 0. \quad (27)$$

This inequality holds for any material at constant temperature and makes intuitive sense, a body subject to free vibration cannot increase its kinetic energy during a cyclic deformation, which imposes restrictions on our elastic materials.

A Cauchy-elastic material is a material where the second Piola-Kirchhoff stress \mathbf{S} is a function of the Green strain \mathbf{E} , $\mathbf{S} = \mathbf{S}(\mathbf{E})$, so obviously all three materials we consider here are elastic. Now, if there exists a cyclic deformation for which $\Delta K < 0$, i.e., strict inequality holds in (27), then obviously this deformation reversed will result in $\Delta K > 0$ because of the presumed elasticity. Consequently an elastic material *must* satisfy

$$\oint \int_{\Omega_0} \mathbf{S} : \dot{\mathbf{E}} d\Omega_0 = 0 \quad (28)$$

for any cyclic deformation. This is one of the definitions of a hyperelastic material and thus the elastic formulations FORM=14 and Stress Map are thermodynamically invalid. This theoretical analysis also provides an understanding of what is going on in our simulations. When the airbags are fully pressurized there is no further external energy input but the systems are under free vibration. For the non-hyperelastic materials elements are likely deforming in cycles that generate kinetic energy and thus cause erratic behaviour. So theory and practice are in agreement, elastic materials must be hyperelastic.

4.2 Hysteresis Model

From a thermodynamical standpoint, pure elastic materials do not exist in practice but all are somehow subjected to dissipation. From the observations in Section 4.1, this seems to not only be of theoretical interest but is also important for numerical stability in transient simulations. We should at this point mention that Rayleigh damping is available in the fabric material models, but this has not been powerful enough to render stability in our simulations. Presumably a problem with numerical damping is the rate dependence, and it can only serve the purpose of stabilizing (almost) hyperelastic materials. Moreover, real life fabric materials display a hysteresis in cyclic loading as shown in Figure 8 and the justification for incorporating rate-independent hysteresis is therefore twofold, physical and numerical.

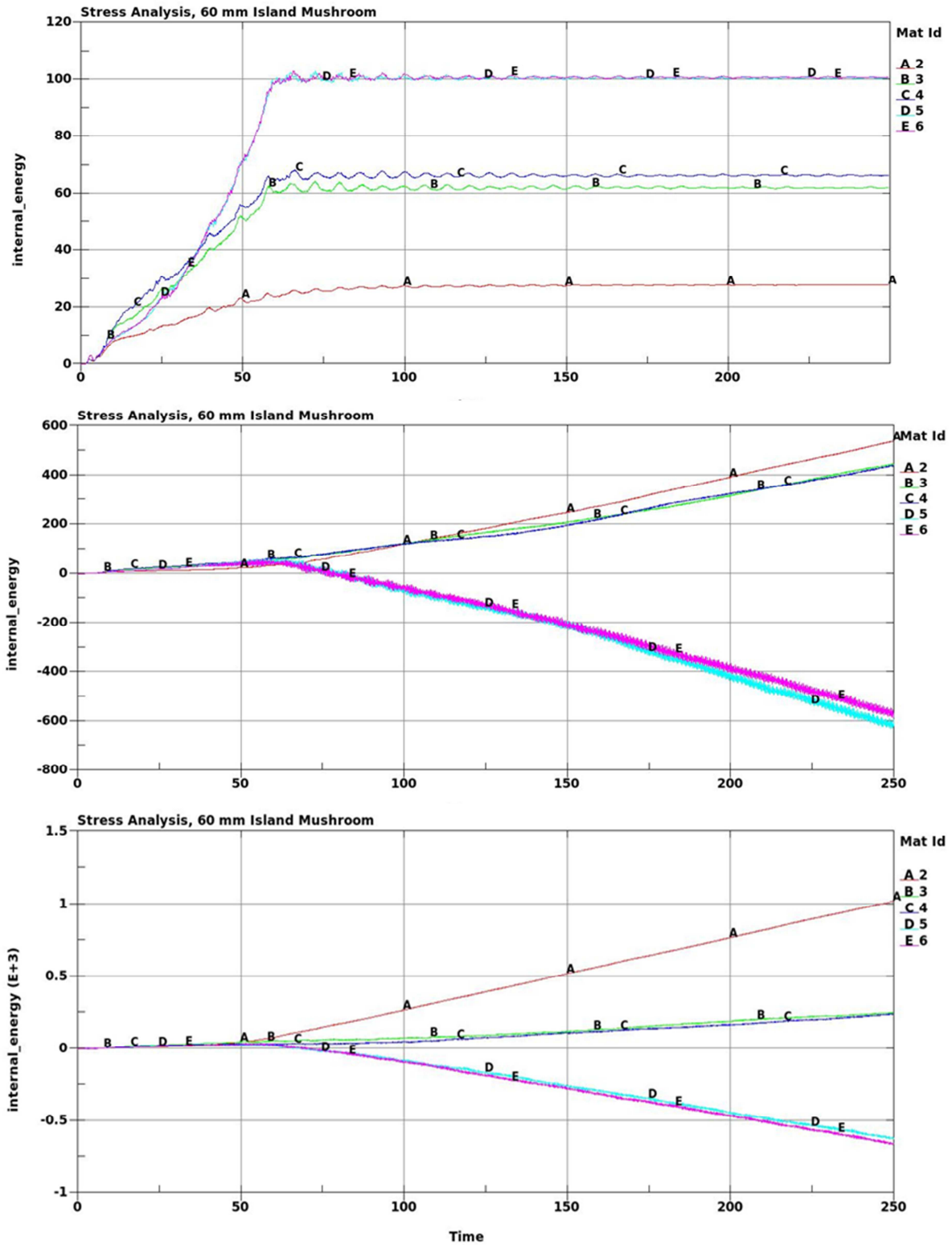


Figure 7 Internal energies by part for the mushroom airbag, FORM=14, FORM=-14 and Stress Map, respectively.

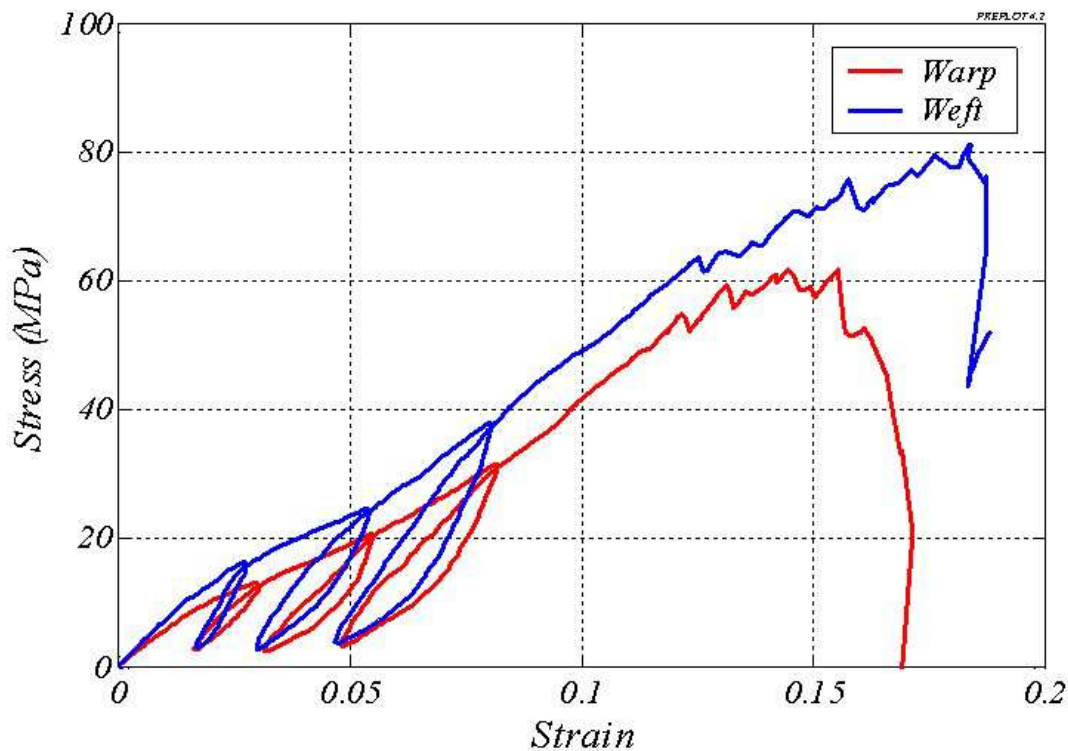


Figure 8 Hysteresis in uniaxial cyclic loading for a typical fabric.

The hysteresis model implemented in the Stress Map Material is based on scaling the elastic stress by a factor γ that evolves with the *stress power*

$$\dot{\epsilon} = \mathbf{S} : \dot{\mathbf{E}}. \quad (29)$$

The nice thing about this quantity is that it can be used to generalize the familiar concepts of *loading* and *unloading* to three dimensional stress-strain states; a material point is under loading if $\dot{\epsilon} > 0$ and unloading if $\dot{\epsilon} < 0$. The evolution of γ is thus related to the stress power in the sense that it will increase during loading and decrease on unloading, quickly enough to introduce the dissipation sought. The exact mathematical formula for γ is complicated, but in essence the function looks like

$$\gamma = \begin{cases} 1 - H + H \exp[\beta(\epsilon - \bar{\epsilon})] & \dot{\epsilon} < 0 \\ 1 - H \exp[-\beta(\epsilon - \underline{\epsilon})] & \dot{\epsilon} \geq 0 \end{cases} \quad (30)$$

where $\bar{\epsilon}$ is the maximum obtained value of ϵ during the simulation and $\underline{\epsilon}$ is the minimum obtained value since the point in time where $\bar{\epsilon}$ was attained. In other words, on unloading γ will exponentially decay to $1 - H$ and on loading it will exponentially grow to 1 and always be restricted by the lower and upper bounds, $1 - H < \gamma \leq 1$. The decay rate β depends on the strain and is determined internally, so the only parameter the user needs is the *hysteresis factor* H . This is determined from the desired amount of dissipation, and with reference to a general loading/unloading cycle illustrated in Figure 9 the relation $1 - H = \epsilon_u / \epsilon_l$ should hold. Note that this model is primarily intended for enhancing numerical stability rather than fitting unloading/reloading data, and numerical experiments have shown that a value of 5% has sufficed to resolve the dynamic instabilities observed in Section 4.1.

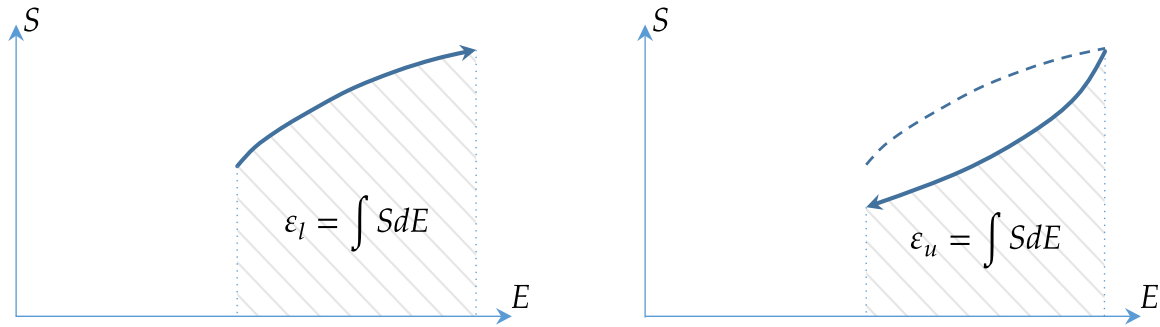


Figure 9 Loading and unloading for determining the hysteresis factor H .

5 Bending

The fabric materials in LS-DYNA use a special membrane element formulation that cannot sustain bending deformation. Pieces of fabrics can therefore fold easily along meshlines without resistance which in turn may result in uncontrollable motion. Furthermore, this precludes the material models from being run implicitly since rigid body modes will be present. As means to remedy these drawbacks, it is possible to coat the fabric with a thin layer of elastic-plastic material, for the following we refer to Figure 10.

Assume that the fabric itself is made up of elements with nodal coordinates x_i and thickness T . Each membrane element has its unique normal \mathbf{m}_j calculated directly from the nodal coordinates, and from this we can calculate unique nodal normals \mathbf{n}_i as some average of the element normals \mathbf{m}_j , $j \in J_i$, where J_i is the index set of elements with node i in its connectivity

$$\mathbf{n}_i = \frac{\sum_{j \in J_i} \mathbf{m}_j}{\|\sum_{j \in J_i} \mathbf{m}_j\|} \quad (31)$$

We can then create virtual coating elements of thickness t located at appropriate offsets from the location of the membrane elements

$$\mathbf{y}_i = \mathbf{x}_i - \frac{T+t}{2} \mathbf{n}_i \quad (32a)$$

$$\mathbf{z}_i = \mathbf{x}_i + \frac{T+t}{2} \mathbf{n}_i \quad (32b)$$

and by using the same connectivity for the two layers we have essentially created a new mesh for each layer. The kinematics of the coating in terms of the variation of nodal coordinates x_i can be determined from the variation of (32) and (31),

$$\delta \mathbf{y}_i = \delta \mathbf{x}_i - \frac{T+t}{2} \delta \mathbf{n}_i \quad (33a)$$

$$\delta \mathbf{z}_i = \delta \mathbf{x}_i + \frac{T+t}{2} \delta \mathbf{n}_i \quad (33b)$$

where

$$\delta \mathbf{n}_i = (\mathbf{I} - \mathbf{n}_i \otimes \mathbf{n}_i) \frac{\sum_{j \in J_i} \delta \mathbf{m}_j}{\|\sum_{j \in J_i} \mathbf{m}_j\|} \quad (34)$$

The variation $\delta \mathbf{m}_j$ can be directly expressed in terms of the global coordinates δx_i , $i \in I_j$, where I_j is the index set of nodes making up the connectivity of element j . With the knowledge of $\delta \mathbf{y}_i$ and $\delta \mathbf{n}_i$ we can employ a shell formulation of choice for the bottom layer, and likewise for the top layer using $\delta \mathbf{z}_i$ and $\delta \mathbf{n}_i$. A Hughes-Liu type shell is used, for which the rate of deformation can be expressed as

$$\delta \boldsymbol{\varepsilon}^y = \mathbf{B}_i^y \delta \mathbf{x}_i \quad (35a)$$

$$\delta \boldsymbol{\varepsilon}^z = \mathbf{B}_i^z \delta \mathbf{x}_i \quad (35b)$$

where the \mathbf{B} matrices contain the information from (33) and (34). The coat material is assumed to be elastic and perfectly plastic with an elastic modulus E and a yield stress σ_Y , and the constitutive law results in coating stresses $\boldsymbol{\sigma}^y$ and $\boldsymbol{\sigma}^z$. The virtual work principle provides the nodal forces by the equations

$$\mathbf{f}_i^y = \int (\mathbf{B}_i^y)^T \boldsymbol{\sigma}^y \quad (36a)$$

$$f_i^z = \int (B_i^z)^T \sigma^z \quad (36b)$$

where it is assumed that the integral is over the bottom and top layer, respectively.

- Membrane element and nodes x_i from input
- - -○ Coated top layer with virtual nodes z_i
- - -○ Coated bottom layer with virtual nodes y_i
- Element normal m_i
- Nodal normals n_i

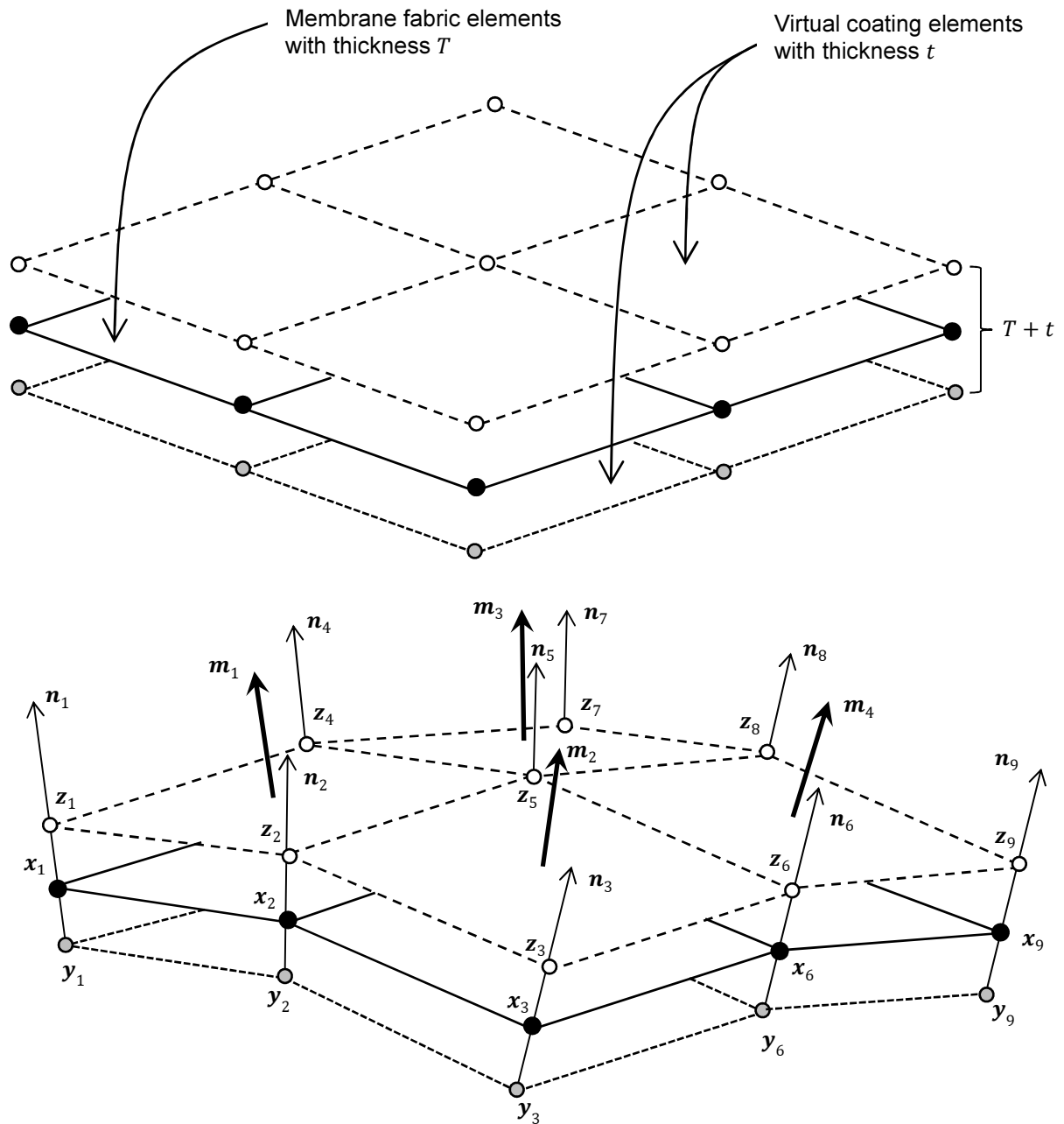


Figure 10 Membrane elements in bending.

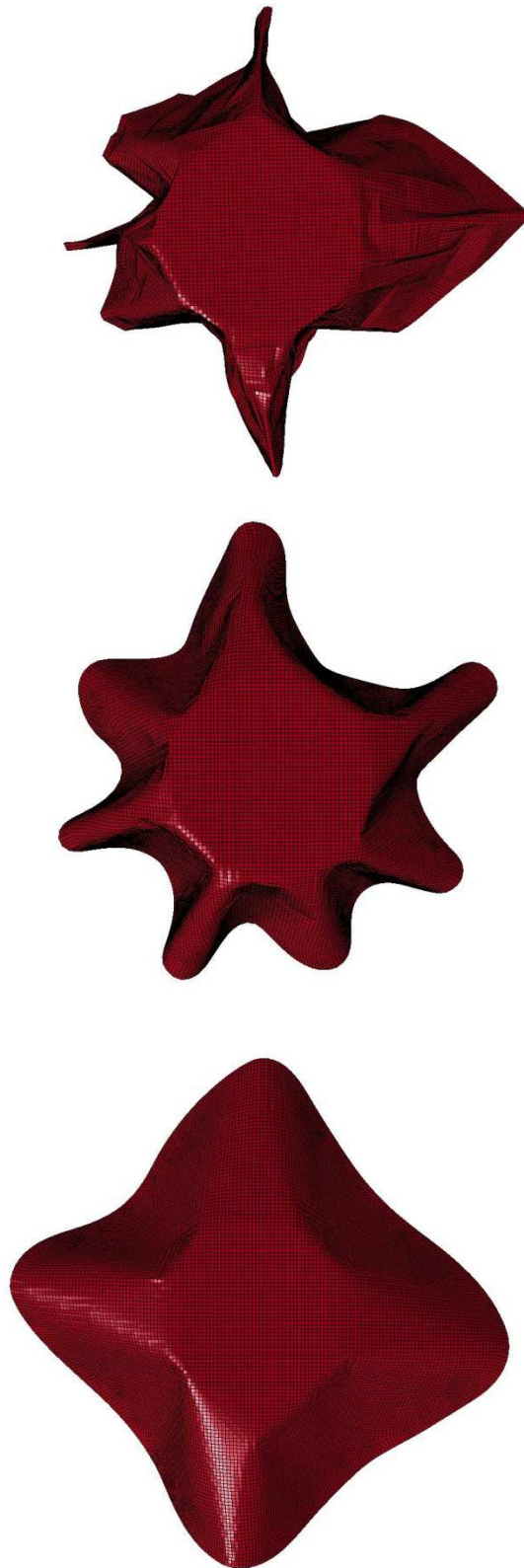


Figure 11 Non-coated and coated fabrics folded onto a cylinder under the influence of gravity.

The effect of applying this technique can be intuitively understood by studying Figure 10, which shows four initially plane membrane elements subjected to an out of plane deformation. If the membrane element side lengths remain constant (solid lines), by design the top layer will be subjected to membrane tension while the bottom layer will be subjected to compression. This result in internal

energy in the coating and the nodal forces will act to prevent this deformation. Another interesting observation is that the force in node 5 in Figure 10 depends on the motion in all of the 9 nodes displayed, which is a necessity due to the lack of rotational degrees of freedom.

In Figure 11 the effect of coating is shown, a fabric is folded onto a cylinder under the influence of gravity. The top figure shows the result without coating, and the wrinkling is quite apparent. The following two figures show the effect of gradually stronger coating, leading to diminished wrinkling tendencies and a seemingly more controlled deformation. The data for the coating, E , σ_Y and t , should be chosen with physics in mind. Material data should presumably correspond to some plastic polymer and the thickness t should not be more than a few percent of the fabric thickness T .

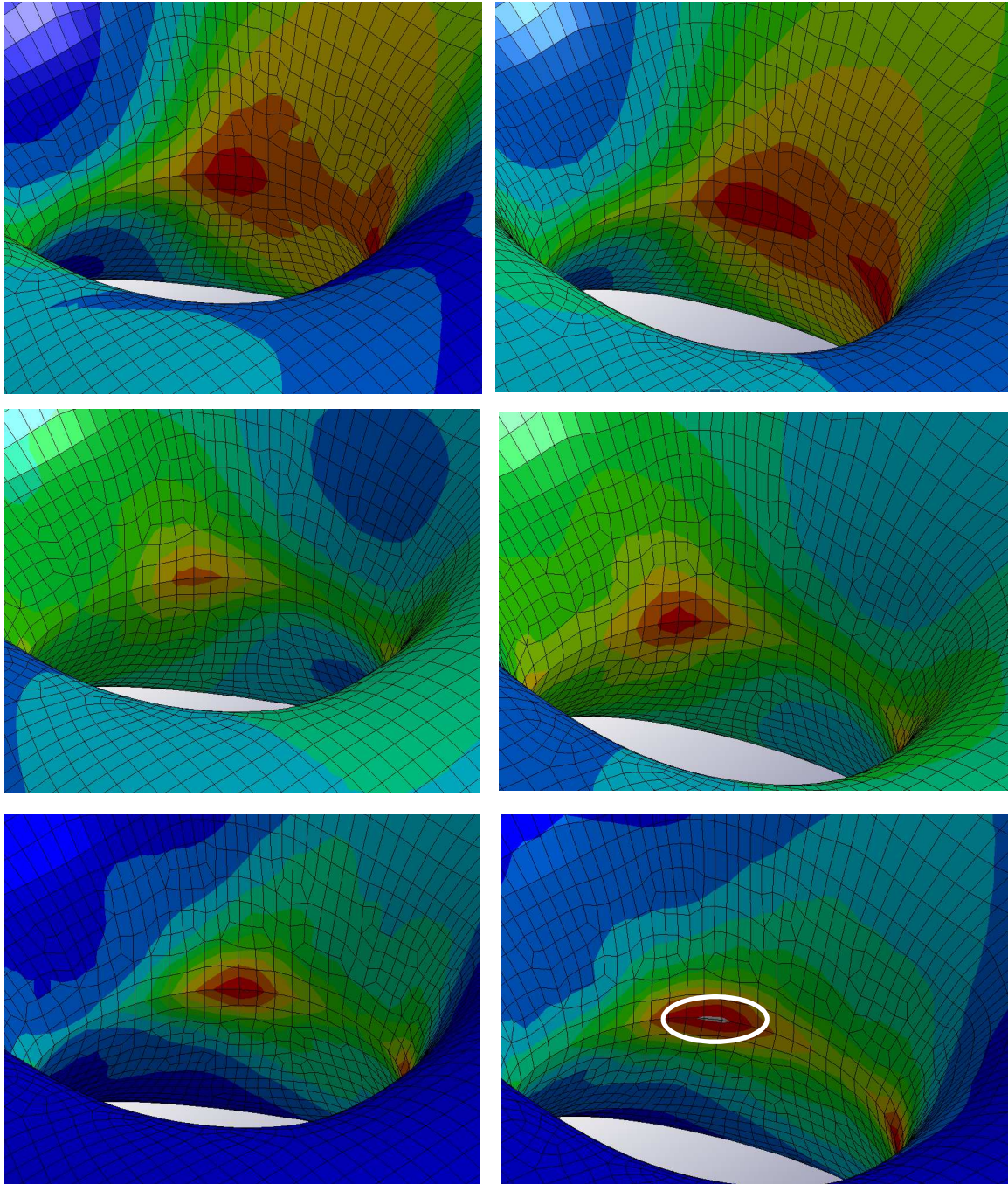


Figure 12 Local region of mushroom cushion for FORM=14 (left) and Stress Map (right). From top to bottom, the a-fiber stress, the b-fiber stress and the failure regions (grey) are shown. A critical seam is highlighted bottom right.

6 Numerical examples

6.1 Predicting Seam Failure

One of the main motivations for the Stress Map model is the need for accurate stress representation to be able to predict seam failure. If considering an airbag mushroom from a system view, it behaves essentially the same regardless if FORM=14, FORM=-14 or Stress Map is used, but there are differences in the local stress and thus the failure/acceptance criterion to potentially impact cushion acceptability.

In Figure 12 this is illustrated for a failure criterion based on the maximum fiber stress. A local region of the mushroom airbag is shown with the fiber stresses colorized with the same contour range. The stress state at the seam between the top and bottom fabric sheets predicts failure for the Stress Map material but not for the FORM=14 material in this case.

6.2 Bending Stiffness Examples

Autoliv airbag fabric materials exhibit bending stiffness due to tightness of weave and / or coating. This stiffness can be approximated using the MAT_FABRIC_MAP material model coating option. Two simple examples were developed to demonstrate this feature: fabric cantilever and fabric loop.

6.2.1 Fabric cantilever

This stiffness can be observed by simply extending a piece of airbag fabric over the edge of a desk or table. The bending stiffness keeps the fabric from collapsing and hanging straight down. This phenomenon can be modeled using the coating feature in the MAT_FABRIC or MAT_FABRIC_MAP material model. This fabric cantilever test was performed and the fabric sag was measured, as shown in Figure 13.

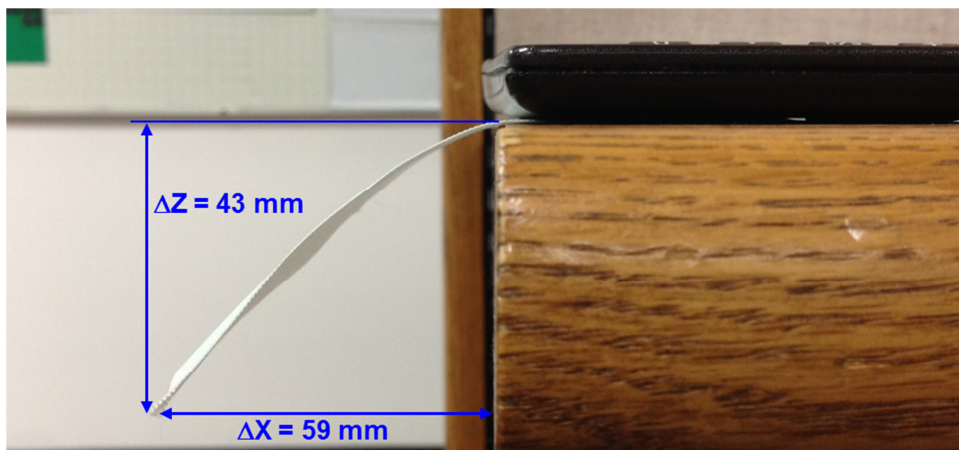


Figure 13 Fabric cantilever test.

A simple rectangular model was developed to demonstrate the effects with and without bending stiffness. First, this model was executed without bending stiffness, as shown in Figure 14. As expected, the fabric hangs straight down without the coating option.

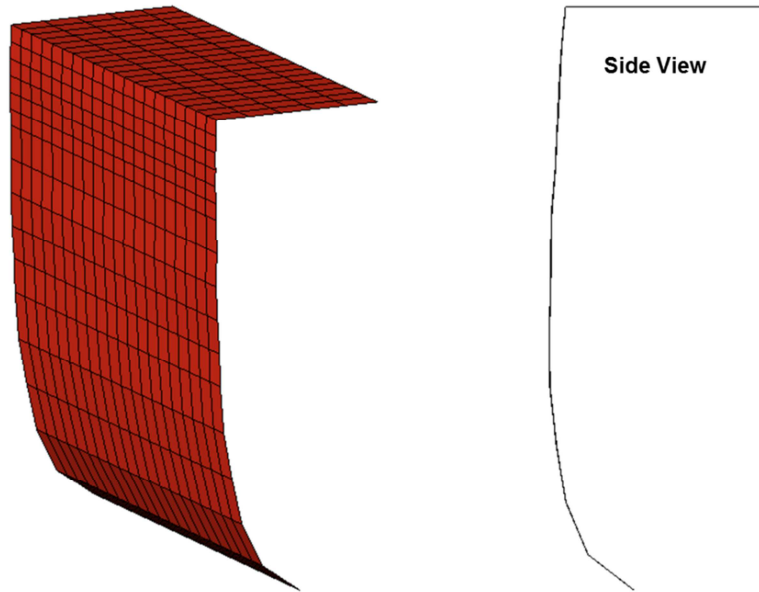


Figure 14 Fabric cantilever model without bending stiffness.

Reasonable values for coating stiffness and thickness were chosen and good correlation with the fabric cantilever test was achieved, as shown in Figure 15.

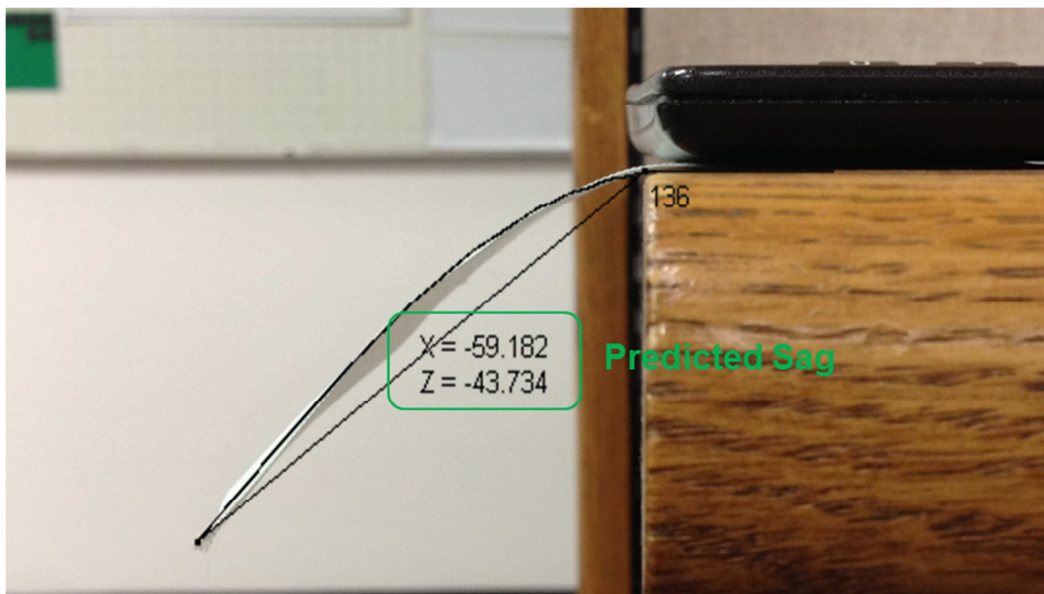
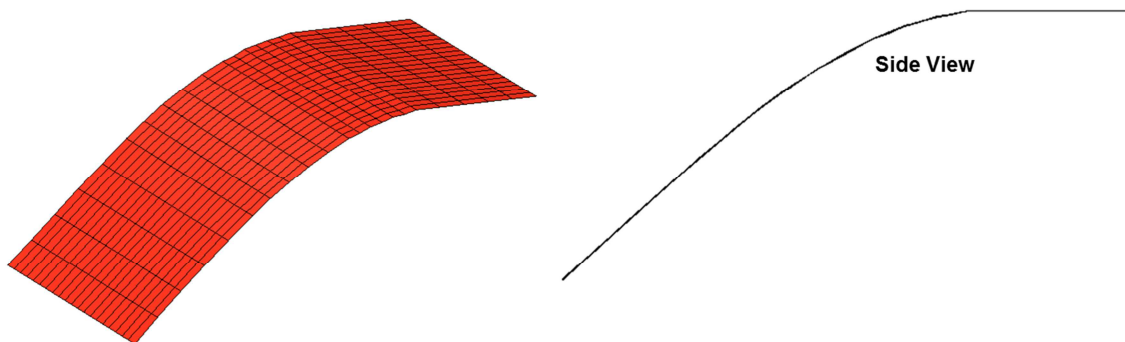


Figure 15 Fabric cantilever correlation.

A simple fabric cantilever test can be accurately modeled with the MAT_FABRIC_MAP material in LS-Dyna.

6.2.2 Fabric loop

Bending stiffness can also be observed by placing a flat piece of fabric on a desk or table and moving the ends together. Because of bending stiffness, the fabric displaces upward and assumes a looping shape, as shown in Figure 16.



Figure 16 Fabric loop test.

This phenomenon can be modeled using the coating feature in the MAT_FABRIC_MAP material model. A simple rectangular model was developed to demonstrate the effects with and without bending stiffness. First, the model was executed without bending stiffness, as shown in Figure 17. As expected, the fabric collapses upon itself.

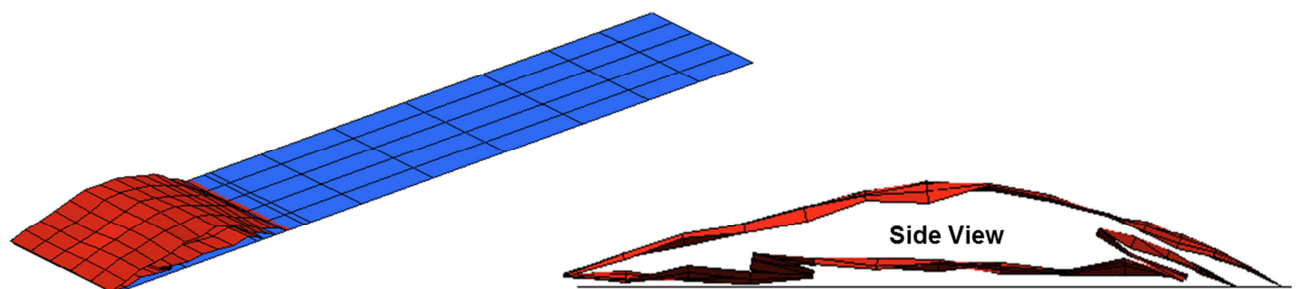


Figure 17 Fabric loop model without bending stiffness.

Values for coating stiffness and thickness were taken from the fabric cantilever model and good correlation with the fabric loop test was achieved, as shown in Figure 18.

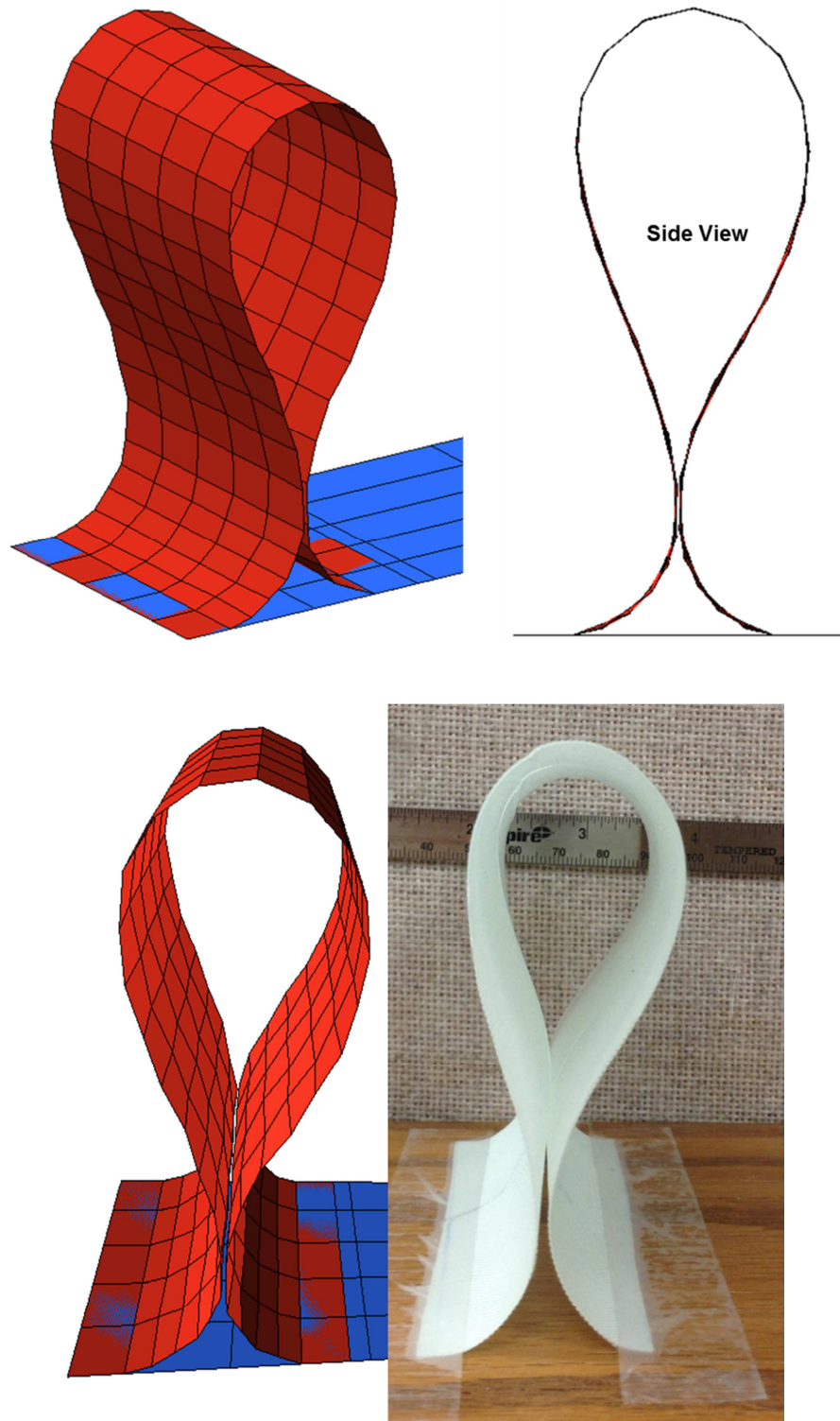


Figure 18 Fabric loop comparison.

These examples show that bending stiffness is required to accurately model airbag fabric behavior. The coating parameters of the MAT_FABRIC_MAP material are an effective way to capture the bending stiffness in a membrane element.

6.3 Fiber Coupling Test

6.3.1 Simplified EjM test

A model was built to represent a hypothetical test to illustrate the fabric stiffness effects due to fiber coupling. This test consists of a standard ejection mitigation head form and a simply supported, unpressurized, circular fabric specimen. The head form is given an initial velocity and a peak

excursion was determined, as shown in Figure 19. This test focuses attention on fabric performance without the complications of pressure or complex boundary conditions. Differences in results can be directly attributed to changes in the fabric stiffness. Various fiber coupling options of the MAT_FABRIC_MAP were compared to the current uncoupled material model, MAT_FABRIC, FORM=14.

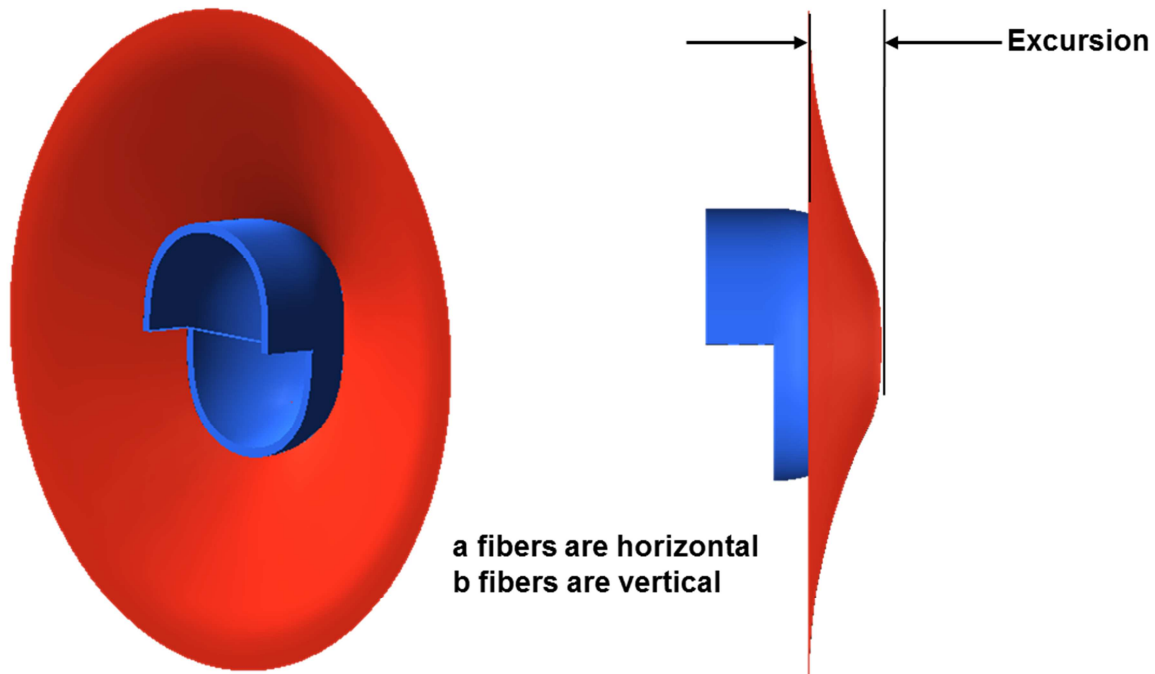


Figure 19 Simplified EJM setup.

Stress maps were developed for the following linear Poisson's ratios, $\nu_{ab} = \nu_{ba} = 0$, $\nu_{ab} = 0.75$ & $\nu_{ba} = 0.3$, $\nu_{ab} = 0.3$ & $\nu_{ba} = 0.75$ and $\nu_{ab} = 0.9$ & $\nu_{ba} = 0.9$. These fiber coupling options were chosen because the results are intuitive. The simulation with Poisson's ratios equal to zero should produce the same results as the FORM=14 material model. The case where $\nu_{ab} = 0.75$ & $\nu_{ba} = 0.3$ was chosen because this is a crude estimation of an actual fabric material based on uniaxial test data. This material should be stiffer and result in less excursion than the uncoupled analyses. The case where $\nu_{ab} = 0.3$ & $\nu_{ba} = 0.75$ was chosen because it should produce the same excursion as the case where $\nu_{ab} = 0.75$ & $\nu_{ba} = 0.3$, due to the symmetry of the setup. The case where $\nu_{ab} = 0.9$ & $\nu_{ba} = 0.9$ was chosen because this is an example of a fabric that is highly coupled. The fabric should be the stiffest material evaluated and result in the least amount of excursion. Bending stiffness (via coating parameters determined in Section 6.2.1) was added to the MAT_FABRIC_MAP materials and the simulations were executed again. These results should be a little stiffer than the models without the coating and should result in lower excursions. The peak excursion results of these simulations are shown in Table 1. The excursion results are very consistent and the MAT_FABRIC_MAP performed as expected.

Table 1 Peak excursion for the simplified EJM model.

Material Model	Excursion (mm)	
	No Coating	Coating
MAT 34, Form=14	156.4	152.8
Stress Map, No Coupling	156.9	153.6
Stress Map, Linear Coupling, 0.75 & 0.3	138.4	136.5
Stress Map, Linear Coupling, 0.3 & 0.75	138.4	136.6
Stress Map, Linear Coupling, 0.9 & 0.9	94.7	94.4

6.3.2 Automotive Safety - Ejection Mitigation Simulation

Ejection mitigation (EjM) is occupant protection in the event of a rollover accident. Data show that serious injury or death are more likely when an occupant is ejected from the vehicle. A countermeasure for this type of accident is an internal curtain airbag (ICAB). The ICAB deploys from the roof trim and covers the window, thus keeping the occupant inside the vehicle. Autoliv manufactures IC airbags and conducts ejection mitigation testing to demonstrate compliance to the US National Highway Traffic Safety Administration's Standard, FMVSS 226.

General EjM testing consists of a linear impactor with a head form that is launched at a pressurized ICAB that is suspended from a car body. The linear impactor and head form mass is 18 kg. Two load cases are performed with different initial head form energies and different airbag pressures.

The result of an EjM test is the amount of head form excursion. Head form excursion is the distance the head form travels past the window inner surface. FMVSS 226 requires the peak head form excursion to be less than 100 mm to pass government testing. Most OEM's require Autoliv to demonstrate excursions less than 80 mm as an added safety precaution.

In 2013, Autoliv conducted a highly controlled and instrumented series of EjM tests using a small scale cushion and an adjustable test fixture instead of a car body, as seen in Figure 20.

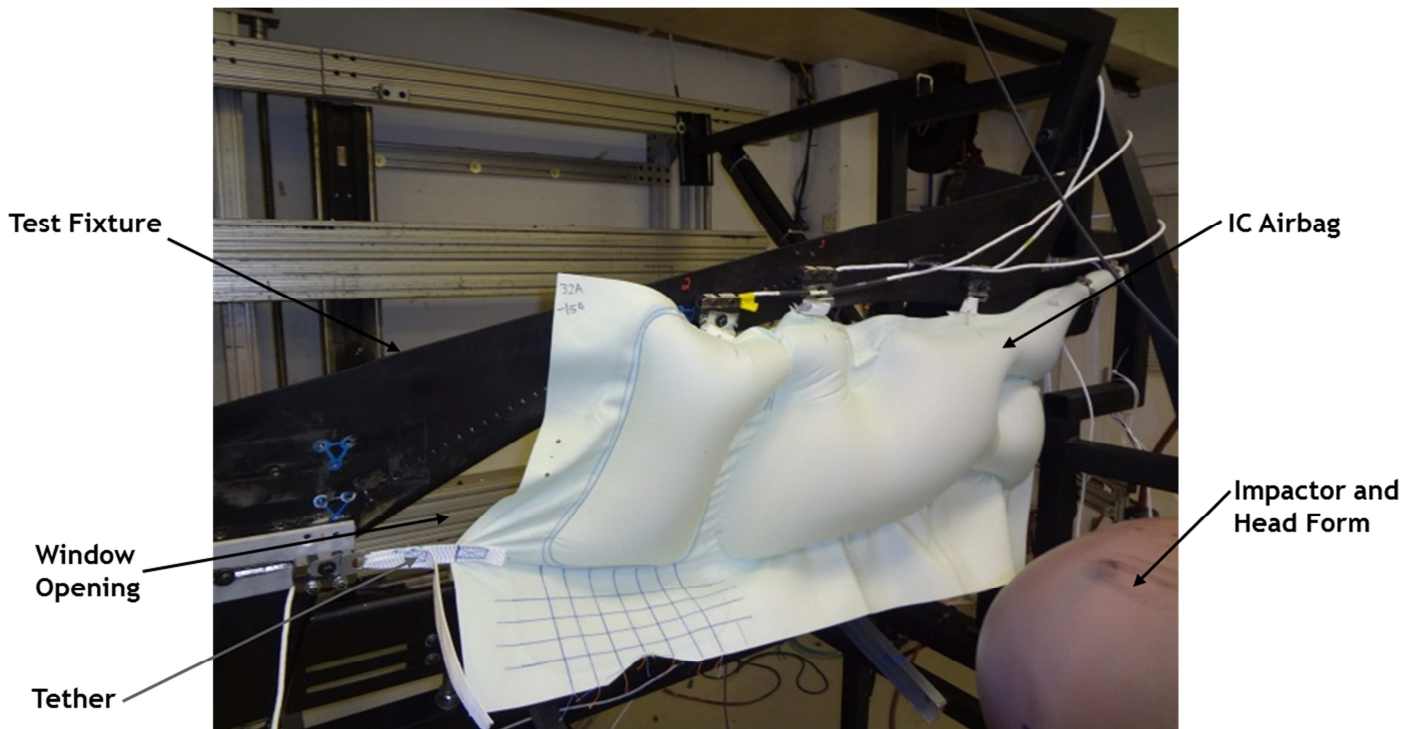


Figure 20 Autoliv test setup.

Initial ICAB pressure was controlled as well as the initial tether tension. A test was repeated several times and an average peak head form excursion of 55 mm was measured.

An LS-Dyna model was built to simulate the testing and predict the head form excursion, as shown in Figure 21.

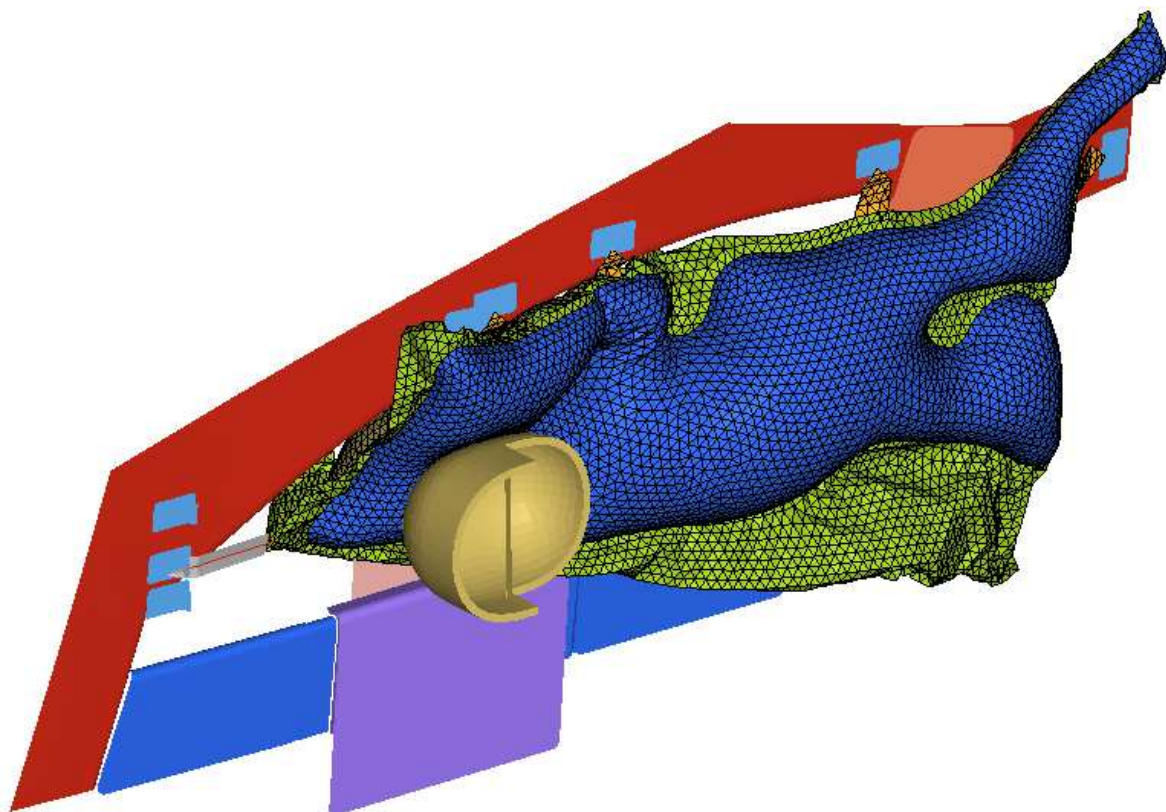


Figure 21 EJM test model.

Using MAT_FABRIC, FORM=14, the peak predicted excursion is 87 mm. Using the equivalent MAT_FABRIC_MAP material model with fiber coupling and the coating option for bending stiffness, the peak excursion was reduced to 57 mm. The FORM=14 excursion would not pass the OEM's requirements and require a redesign of the ICAB. Using the more realistic material model produces an excursion prediction that agrees with the test measurement and passes the OEM EJM requirement.

7 Summary

A thorough investigation of the most common fabric material modeling options in LS-DYNA has been presented, with emphasis on the new Stress Map material. The Stress Map material allows for general in-plane membrane coupling between the fiber stresses and facilitates the assessment of an airbag design from a constructional point of view. A number of additional features have been discussed, including hysteresis, volumetric compaction and bending, that we find necessary to enhance robustness and accuracy in the present model. Numerical examples highlight the effects of these features and also show the potential advantages of incorporating fiber coupling in the simulation of airbag deployment.

8 Literature

- [1] LS-DYNA Keyword User's Manual, Volume I & II, LS-DYNA R8.0, Lawrence Livermore Software Technology Corporation (LSTC), 2015.
- [2] Klarbring A., and Strömberg N., *Topology Optimization of Hyperelastic Bodies including Non-Zero Prescribed Displacements*, Struct. Multidisc. Opt. 47 (2013), pp. 37-48.
- [3] Casey J., *A remark on Cauchy-Elasticity*, Int. J. Non-Lin. Mech. 40 (2005), pp. 331-339.